Effects of sulphurization time on Cu_2ZnSnS_4 absorbers and thin films solar cells obtained from metallic precursors

P. A. Fernandes, P.M.P. Salomé, A.F. Sartori, J. Malaquias, A.F. da Cunha, Bjöm-Arvid Schubert, J. C. González, G. M. Ribeiro

Abstract

We report the results of a study of the sulphurization time effects on Cu_2ZnSnS_4 absorbers and thin film solar cells prepared from dc-sputtered stacked metallic precursors. Three different time intervals, 10 min, 30 min and 60 min, at maximum sulphurization temperature were considered. The effects of this parameter' change were studied both on the absorber layer properties and on the final solar cell performance. The composition, structure, morphology and thicknesses of the CZTS layers were analysed. The electrical characterization of the absorber layer was carried out by measuring the transversal electrical resistance of the samples as a function of temperature. This study shows an increase of the conductivity activation energy from 10 meV to 54 meV for increasing sulphurization time from 10 min to 60 min. The solar cells were built with the following structure: SLG/Mo/CZTS/CdS/i- ZnO/ZnO:Al/Ni:Al grid. Several ac response equivalent circuit models were tested to fit impedance measurements. The best results were used to extract the device series and shunt resistances and capacitances. Absorber layer's electronic properties were also determined using the Mott-Schottky method. The results show a decrease of the average acceptor doping density and built-in voltage, from 2.0×10^{17} cm^{-3} to 6.5×10^{15} cm^{-3} and from 0.71 V to 0.51 V, respectively, with increasing sulphurization time. This results also show an increase of the depletion region width from approximately 90 nm to 250 nm.

Keywords

Cu_2ZnSnS_4, CZTS, absorber, sulphurization, thin film, solar cell

1. Introduction

The search for alternative semiconductor compounds to replace $Cu(In,Ga)Se_2$ (CIGS) as the absorber layer in thin film solar cells has accelerated in recent years. The quaternary metal sulphide, Cu_2ZnSnS_4 (CZTS) seems to gather important properties which suggest that it could be a possible replacement. This compound is constituted by low cost and non toxic elements. CZTS is a p-type semiconductor with an absorption coefficient higher than 10^4 cm^{-1} and a band gap close to 1.5 eV [1–3]. Despite these interesting optical properties the best conversion efficiency attained so far with CZTS based solar cells was 8.4% [4], which is a modest value compared with the 20.3% reached by CIGS, [5]. Such low efficiency can be partially attributed to the difficulties of the synthesis of the absorber layer, and as suggested by Chen *et al.* [6], the formation of stoichiometric CZTS has a very narrow chemical potential region. These growth problems are more evident considering that the best solar cell results are attained using non stoichiometric absorber layer compositions such as Cu poor and Zn rich precursors, according to Katagiri *et al.* [7]. This means that unless very controlled conditions are met, unwanted phases, like ZnS, Cu_2SnS_3, $Cu_{2-x}S$ among others [2, 8], could easily remain after the completion of the sulphurization/crystallization process.

Several techniques were developed to grow the Cu_2ZnSnS_4 compound. This process can be divided in 2 parts. The first part refers to the deposition of the precursors which can be done by vacuum or by non-vacuum methods. Vacuum methods, like thermal and sequential e-beam evaporation were tested by Friedlmeier *et al.* [9] and Katagiri *et al.* [10], respectively. The co-evaporation was performed by Tanaka *et al.* [11] using metallic precursors and by Bjöm-Arvid Schubert *et al.* [12] using copper, tin and zinc sulfide sources. Sputtering techniques were tested in different configurations: sequential deposition of metallic precursors [8, 13] and co-sputtering of binary sulphide precursors [14]. Non-vacuum methods include electrodeposition [15, 16], chemical bath deposition [17] and spray pyrolysis [18, 19]. For the second part, the methods used differ on the sulphurization conditions, which can be performed in a sealed environment [19] or using a transport gas, such as Ar or N_2 [13, 15]. The sulphurization can also be done using sulphur vapour or H_2S [13, 15, 16]. Different maximum sulphurization temperatures were tested with the published data ranging from 500 °C to 600 °C. Relatively high pressures have been tested in order to decrease the losses of Zn and Sn during the sulphurization process.

In this work we show the results of a set of experiments on the properties of the CZTS layer and the solar cells derived from them aimed at studying the effect of the sulphurization time. This work shows the compositional, structural and morphological changes of the CZTS layer when the samples are subjected to different sulphurization times. Electrical characterization of the CZTS layers and final solar cells was performed and the results are also discussed.

2. Experimental details

2.1. Sample preparation

The method used for the growth of the absorber layer consisted in the sequential deposition of metallic precursor layers done by dc magnetron sputtering and a final annealing /sulphurization process, allowing the formation of the CZTS compound [8].

Successive ultrasonic baths of acetone/ethanol/deionised water and subsequent N_2 flow were applied to a 3×3 cm^2 soda-lime glass (SLG) substrate as the cleaning and drying process, respectively. Next, the deposition of Mo back contact was performed by dc magnetron sputtering from a Mo target with 3N purity as described by Salomé *et al.* [20]. The metallic precursors were deposited sequentially using dc magnetron sputtering. The deposition order used was SLG/Mo/Zn/Sn/Cu [13]. All depositions were done under an Ar atmosphere, with an operating pressure of 2×10^{-3} mbar, and the power densities used for Cu, Zn and Sn were 0.16 Wcm^{-2}, 0.36 Wcm^{-2} and 0.11 Wcm^{-2}, respectively. The distance between the target and the sample was 8 cm. The purity of the targets was 5N for Cu and 4N for both Zn and Sn. In situ thickness' monitoring was performed with a quartz crystal monitor.

The formation of the CZTS layer was performed in a tubular furnace in a N_2 plus sulphur vapour atmosphere at a constant working pressure of 5 mbar and a N_2 flow rate of 40 ml/min. The sulphur pellets, with purity 5N, were evaporated at 130 °C in a temperature controlled quartz tube source. The furnace temperature was ramped up at 10 °C/min until the maximum sulphurization temperature of 520 °C was attained. This temperature was kept constant during 10 min, 30 min and 60 min and then the system was set to cool down naturally. These profiles are sketched in Figure 1.

Secondary phases, such as $Cu_{2-x}S$, that form during the CZTS crystallization process were eliminated using a KCN chemical treatment [13]. The samples were, sequentially, subjected to the KCN solution at 10% w/w, a solution of ethanol/deionised water at 50% vol/vol and finally deionized water. Each step had the duration of 2 min. Finally, all samples were dried with a N_2 gas flow.

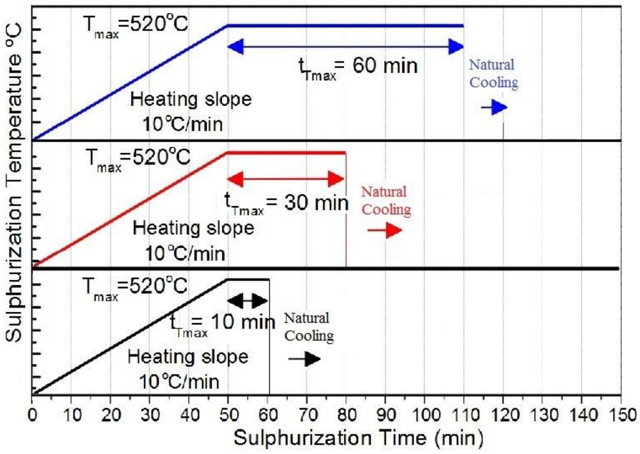

Figure 1: Sulphurization profiles used for the growth of the CZTS layer.

Electrical resistance measurements of the CZTS layers were carried out in order to understand the influence of the sulphurization time over the transport properties of the samples. For these measurements the Mo layer deposited between the SLG substrate and the CZTS layer was used as a back contact, while a C-shaped gold electrode was thermally evaporated on top of the CZTS film and used as the top electrical contact. In this contact configuration the transversal transport across the cross-section of the CZTS layers was measured.

For the preparation of solar cells an n-type CdS layer was deposited by the chemical bath method. The process allows the formation of a hetero-junction with the p-type CZTS. Next, an i-ZnO/ZnO:Al window layer was deposited by RF-magnetron sputtering. Finally, Ni/Al metal grids were deposited by e-beam evaporation through an aperture mask to form the front contact.

2.2. Sample characterization

In situ thickness monitoring was done using a quartz crystal system during the metallic precursor deposition. A Dektak 150 step profiler was used to measure the thickness of individual metallic precursors and the final CZTS layer thicknesses. X-ray diffraction (XRD) analysis was performed with a PHILIPS PW 3710 system equipped with a Cu-Kα source (wavelength λ=1.54060 Å) and the generator settings were 50 mA, 40 kV. Surface Scanning Electron Microscopy (SEM) and energy dispersive X-ray spectroscopy (EDS) compositional analysis were perform using a Hitachi S4100 SEM and a Rontec EDS with setting parameters of 25 kV and 10 µA. A Hitachi Su-70 was used for cross-sectional SEM micrograph acquisition with setting of 7 kV and 30 µA. Raman scattering measurements were performed in the backscattering configuration and the excitation laser line used was 488 nm. The Jobin-Yvon T64000 Raman spectrometer was equipped with an Olympus microscope with a 100x magnification objective lens. It focused the laser beam down to a spot size of 1 µm in diameter. This equipment has a resolution of 1 cm^{-1}. The compositional analysis was complemented using Inductively Coupled Plasma - Mass Spectrometry (ICP-MS) measurements with a Jobin-Yvon Activa-M

Param.	S10(prec.)	S30(prec.)	S60(prec.)
[*Cu*]/([*Zn*] + [*S n*])	0.9±0.1	0.9±0.1	0.9±0.1
[*Zn*]/[*S n*]	1.4±0.2	1.3±0.1	1.3±0.1

Table 1: Composition ratios for metallic precursors measured by ICP-MS.

		S10	S30	S60
$\frac{[Cu]}{[Zn]+[Sn]}$	top	0.9±0.2	0.8±0.1	0.9±0.1
	back	0.6±0.1	0.7±0.1	0.8±0.1
$\frac{[Zn]}{[Sn]}$	top	1.6±0.3	1.4±0.3	1.4±0.3
	back	2.1±0.4	1.3±0.3	1.5±0.3
$\frac{[S]}{[Zn]+[Sn]+[Cu]}$	top	1.1±0.4	1.0±0.3	1.1±0.3
	back	-	-	-

Table 2: Composition ratios of the CZTS layer measured by EDS. The results include the measurements observed from top and back CZTS surface layer.

system. Sample preparation for ICP analysis follows the standard procedure that includes dissolving the films using a solution of aqua regia, nitric acid and hydrochloric acid in a volume ratio of 1:3 at temperature of 80 °C. Electrical resistance measurements were done under dark conditions as a function of temperature in the 10 K - 310 K range. The samples were mounted in an Oxford Instrument SpectrostatCF static continuous flow cryostat CF104, especially modified to allow low noise electrical measurements of the samples, and the electrical measurements were done with a 237 high voltage source-measure unit from Keithley. Special care was taken in confirming that the contacts were ohmic over the entire temperature range by acquiring current-voltage curves. Current-voltage characteristics of the solar cells were measured under illumination in simulated standard test conditions: AM1.5 and 1000 W/m^2. A calibrated Si-cell was used as reference for the J(V). Admittance measurements were carried out under dark conditions at room temperature using a 4 point probe setup and a HP42805A (75 KHz-30 MHz) impedance analyser. The amplitude of the ac signal was set to be constant and equal to 25 mV.

The samples are identified according to the sulphurization time (in minutes).

3. Results and Discussion

3.1. *Compositional characterization*

In Table 1 it is shown the composition ratios for the precursors measured with ICP-MS. This method was used due to the fact that EDS analysis is not suitable for stacked layers configuration. The composition of the precursors was Cu-poor and

Sample	Zn (µm)	Sn (µm)	Cu (µm)	Prec. (µm)	Abs. (µm)	Δ (%)
S10	0.86	1.05	0.47	2.38	3.30	38
S30	0.70	0.97	0.38	2.05	2.90	41
S60	0.74	1.08	0.40	2.22	2.70	22

Table 3: Thicknesses of individual metallic layers and final metallic precursors measured by step profiler. Thicknesses of CZTS absorber

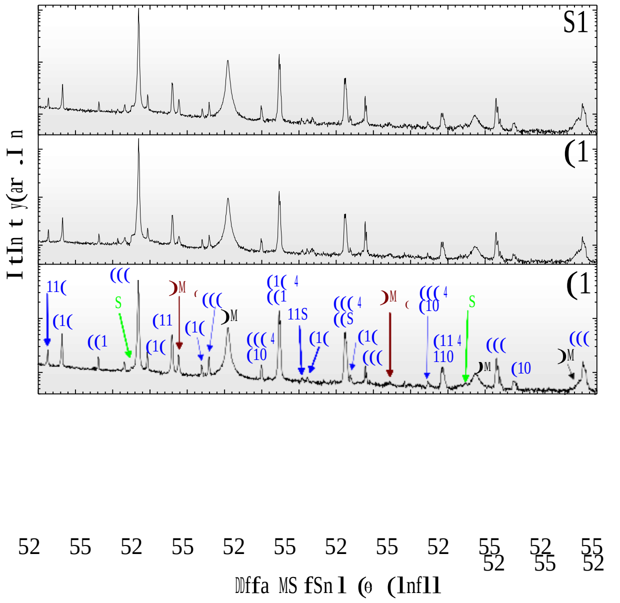

Figure 2: XRD diffractograms of the samples S10, S30 and S60. The peaks and crystal planes assignments were done using ICDD database [24] for CZTS, Mo, MoS_2, SnS and Cu_xSn_y.

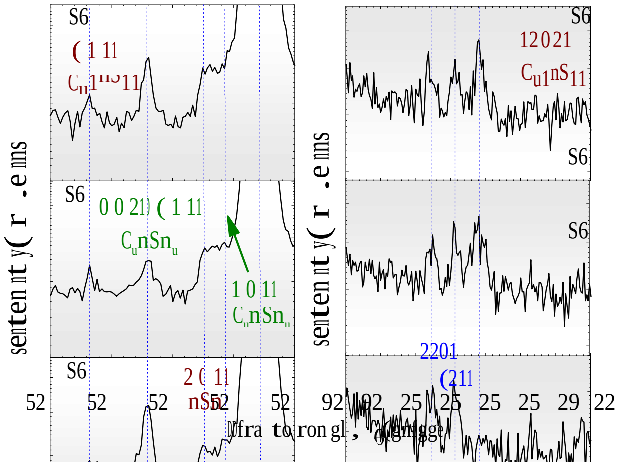

Figure 3: Details of the XRD diffractograms of the samples S10, S30 and S60 at 2θ close to 27° and 51°. The peaks and crystal planes assignments were done using ICDD database [24] for CZTS, $Cu_{41}Sn_{11}$, Cu_4SnS_4 and SnS.

layer measured by cross-sectional SEM micrograph. The estimation of the relative volume variation, Δ, between precursors and CZTS layer.

Zn-rich which follows the recommendation by Katagiri *et al.* [7] for improved solar cell performance. Some residual composition variation is observed but it remains within the uncertainty interval.

Table 2 shows the results of the final compositional analyses of the samples. These results were measured using the EDS technique. Considering the limited penetration depth of EDS, we present the results measured from top and back surfaces of the CZTS layer. We exposed the latter detaching the CZTS layer from the Mo/MoS_2 layer using an adhesive tape. By comparing these results, it can be seen that the element inter-diffusion is not complete, especially for a sulphurization duration of 10 min. This is demonstrated by the ratio $\frac{[Cu]}{[Zn]+[Sn]}$ for top and back surfaces, of 0.9 and 0.6, respectively, and $\frac{[Zn]}{[Sn]}$ for top and back surfaces, of 1.6 and 2.1, respectively. For the other samples these differences seem to be smaller and a higher compositional uniformity is observed. Although the ICP-MS analysis is more accurate than EDS, we used the latter because it preserves some spatial information of the composition. In ICP-MS the samples are dissolved in an acidic solution, losing all information about the compositional spatial distribution. To avoid the influence of the Mo of the back contact in the measurement of the S content of the absorber layer, the top surface measurements were not presented in the table 2. Only the back surface measurements are presented. Note that the EDS analysis presents problems to distinguish the Mo from the S due to the proximity of the X-ray emission lines. Cross sectional EDS mapping (not shown) present not significant signal variation for the sulphur element from the middle to top region of the absorber layer. The ratios $\frac{[S]}{[Cu]+[Zn]+[Sn]}$ shown in table 2 with values close to 1.0 suggest that the samples are almost completely suphurized, although the presence of residual poor sulphur phases, as shown in section 3.2.

Table 3 shows the results of the thickness measurements of the individual metallic precursors, the final precursor layer and the CZTS layer. The measurements of the CZTS layer thickness was performed by cross-sectional SEM micrographs, shown in Figure 6. It is also included the estimation of the volume variation of the sample before and after the sulphurization process. It is seen that sample S60, which has undergone a longer sulphurization process, shows a lower volume increase, indicating possible material losses or a higher film compactness. These losses are mainly in the form of SnS by re-evaporation [8]. This fact can explain the higher $\frac{[Zn]}{[Sn]}$ ratio for the CZTS layer when compared with the precursor layer shown in Table 2. The comparison between sulphurized samples can be misleading because the loss effect is masked by a compositional uniformity increase.

3.2. Structural characterization

For the structural analysis and phase identification we used two techniques, namely, XRD and Raman scattering. The need for the complementarity of these techniques is related to the fact that CZTS, cubic-ZnS and cubic-Cu_2SnS_3 (CTS) have very similar unit cell structures [2, 21]. This results in similar XRD diffractograms. The Raman scattering technique can resolve those phases [22, 23].

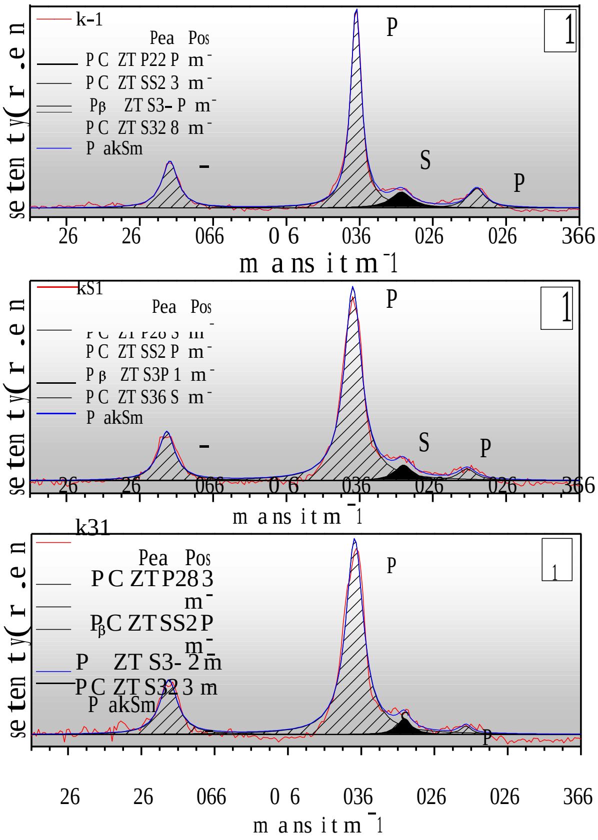

Figure 4: Raman scattering spectra of the samples S10, S30 and S60. These measurements were performed on the top surface of the CZTS layer. The CZTS peak assignments were done according to [8, 25]. Experimental points were fitted using Lorentzian curves. The deconvolution of shoulder at 350 cm^{-1} allowed the detection of the β-ZnS phase located at 352 cm^{-1} [22].

In Figure 2 the XRD diffractograms of the samples are shown. The analysis of these diffractograms was complemented with the Raman scattering data shown in Figure 4 and Figure 5. CZTS peak assignment and crystal plane identification are presented in Figure 2 for sample S10 [24]. The Mo [24], binary sulphides MoS_2 [24] and SnS peaks [24] are also visible in all the diffractograms. Figure 3 presents the zoomed in XRD results for 2θ close to 27° and 51°. From these diffractograms, it seems that samples S30 and S60 present additional peaks assigned to an intermetallic binary compound $Cu_{41}Sn_{11}$ [24]. Despite the peak intensities suggesting that this compound is present at residual level, this is an unexpected result for longer sulphurization processes. These XRD results also suggest the presence of the ternary compound Cu_4SnS_4 [24] for all the samples.

Raman scattering results for the top surface of the absorber layer are shown in Figure 4. The penetration depth of these measurements, considering the excitation wavelength used, 488 nm, is expected to be close to 140 nm [22]. According to the graphs, the absorber layer is constituted mainly by the CZTS phase [8, 25]. All peaks were fitted using Lorentzian curves in order to pin point their location and to deconvolute the shoulder close 350 cm^{-1}. This allowed the detection of the β-ZnS phase located at 352 cm^{-1} [22].

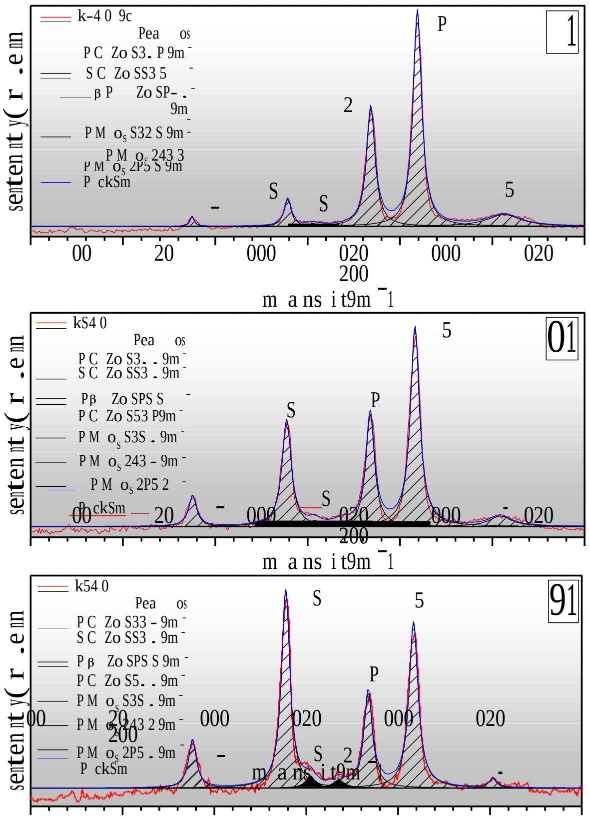

Figure 5: Raman scattering spectra of the samples S10, S30 and S60. These measurements were performed on the back surface of the CZTS layers. The peak assignments were made according to published references [8, 22, 25, 26].

In Figure 5 the Raman scattering spectra of the CZTS layers measured from the back side are presented. The curves were fitted using the same procedure as for the results presented in Figure 4. Figure 5 shows additional peaks which correspond to the MoS$_2$ according to Sandoval *et al.* [26]. As expected, these results also present the peak assigned to the β-ZnS phase. Although, for the sample S10, it would be expected a higher peak intensity due to the fact that the composition is more Zn-rich than the other samples. The intense MoS$_2$ peaks could hide the β-ZnS lower intensity one. Additionally, the use of the 488 nm laser radiation wavelength for the Raman scattering measurements is not appropriate to study the peak intensity with the phase amount for high band gap energy materials [23].

According to the pseudo ternary diagram presented by J. Scragg [27], the composition analyses of both back and top surface place the results close to a region where it is expected the formation of CZTS + ZnS and CZTS + ZnS + Cu$_2$S. The phase Cu$_2$ZnSn$_3$S$_8$ was never detected in our samples, so it is not considered. The Cu$_2$S is removed using KCN based etching process. These results were confirmed by complementary structural analysis based on the XRD and Raman scattering. Furthermore, the combination of the results of the composition with the structural analysis suggests that, despite the overall composition tends to be more uniform with the increase of the sulphurization time, observed by convergence of composition ratios in table 2, the growth conditions used do not guarantee that all compositional inhomogeneity spots are eliminated. These local conditions promote the formation residual phases SnS and Cu$_4$SnS$_4$. In fact, the increase in of sulphurization time seems to promote the formation of the intermetallic phase, Cu$_{41}$Sn$_{11}$, although in trace amounts, as shown in the diffractograms of Figure 3.

Table 4 shows the position and FWHM of the CZTS XRD main peaks. The sizes of the crystallites were estimated according the Scherrer's equation [28]:

$$Size = \frac{4}{3}\frac{K\lambda}{B_{1/2}cos\theta_B} \qquad (1)$$

where λ is the radiation wavelength, K is an unit cell geometry dependent constant, which was set to be equal to 0.99, $B_{1/2}$ is the corrected FWHM of the main XRD peak, θ_B is the XRD peak position and 4/3 refers to a geometrical correction assuming spherical crystallite shapes. From these results, it is clear that XRD results point to an increase in the crystallinity of the samples given the increase of the crystallite size, rising from ∼120 nm for S10 to ∼210 nm for S60. The FWHM were extracted from the diffractograms and corrected for the overall XRD equipments peak broadening of 0.110. This is obtained using high quality standard LaB$_6$ sample to minimize the broadening effect of finite crystallite sample. The corrected FWHM was estimate according the expression:

$$B_{1/2} = \sqrt{FWHM^2 - corr^2} \qquad (2)$$

where *corr* is the correction parameters related to the equipment's peak broadening.

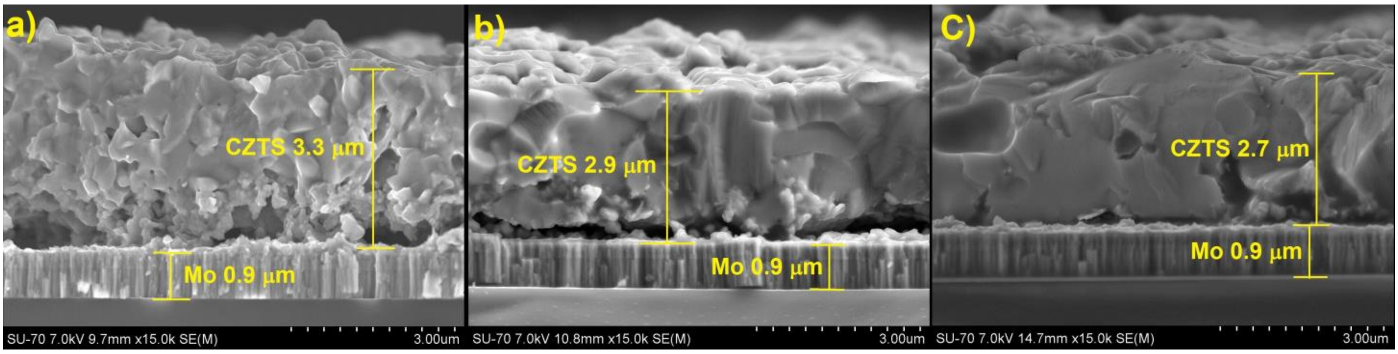

Figure 6: Cross-sectional SEM micrograph for samples a) S10, b) S30 and c) S60.

Sample	Peak Pos.	FWHM	$B_{1/2}$	Size (nm)
S10	28.46°	0.225°	0.098°	120
S30	28.46°	0.170°	0.065°	190
S60	28.45°	0.159°	0.057°	210

Table 4: Position and FWHM of the main peaks of CZTS measured by XRD. Estimation of the crystallite size, according to the Sherrer's equation [28], for the samples S10, S30 and S60.

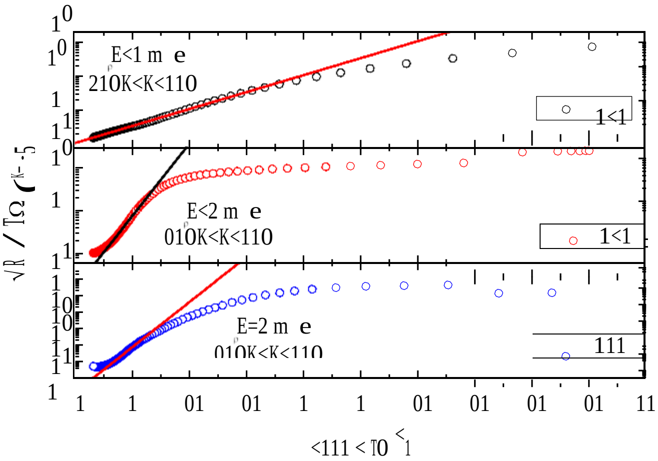

Figure 7: $\frac{R}{\sqrt{T}}$ vs. $\frac{1000}{T}$ curves for samples S10, S30 and S60.

3.3. Morphological characterization

The cross-sectional SEM micrographs for the studied samples are shown in the Figure 6. The micrographs a), b) and c) refer to samples S10, S30 and S60, respectively. Smaller grains are seen in sample S10 than in the other two samples. This Figure also shows the thickness estimation of the various layers. In Figure 6 a) it is clear that a layer between the CZTS and the Mo back contact exists and it is constituted by small grains. This is also observed in Figures 6 b) and 6 c), though to a smaller extent.

3.4. Electrical characterization of the CZTS layer

The electrical characterization of the CZTS thin films was carried out by measuring the transversal electrical resistance $R(T)$ of the samples as a function of temperature. Hot point probe measurements were also carried out, showing that the samples present p-type conductivity. The p-type conduction has also been observed by Hall effect measurements in samples grown under very similar conditions [29]. Figure 7 shows the $R/\sqrt{T}$ vs. $1000/T$ curves for samples S10, S30 and S60. Three different regimes can be observed in these curves, namely, at high temperatures, moderate temperatures and low temperatures. In the high temperature region $R(T)$ saturates, probably due to the full ionization of the acceptor centers in the samples. In a previous paper [29] we have shown that similar CZTS samples present a shallow acceptor with a 29 meV ionization energy. At moderate temperatures, the $R/\sqrt{T}$ vs. $1000/T$ curves exhibit an Arrhenius behavior with a characteristic activation energy, E_ρ. E_ρ defines the activation energy of the grain-boundary-limited conductivity and depends on the ionization energy of the acceptors as well as the barrier height between grains [30]. The values of E_ρ, as well as the temperature interval in which the Arrhenius behavior was observed, are shown in Figure 7. It is important to note that the increase in the sulphurization times leads to an increase in E_ρ. This apparently contradictory behavior, with the increase of the grain size, could be explained by changes in the electronic properties. The increase of the interdiffusion of metallic elements can promote the formation of defects with a deeper transition energy, thereby changing the conductivity of the absorber layer and masking the effect of grain size. At low temperatures the Arrhenius behavior is not followed. Electrical conductivity measurements carried out in similar CZTS thin films, but grown without the Mo layer, have shown that the low temperature electrical transport is dominated by Variable-Range Hopping (VRH) conduction. Although VRH has not been observed in the samples studied in this work, it could be one of the mechanisms contributing to the $R/\sqrt{T}$ vs. $1000/T$ curves at low temperatures. The formation of a Schottky barrier at the Mo/MoS$_2$/CZTS interface [4] can also strongly modify the electrical transport of the samples measured here with respect to pure CZTS thin films.

3.5. Impedance spectroscopy

The electrical characterization of the best solar cell of each tested sample was done through impedance spectroscopy and the J-V characteristics at room temperature. From now on the best cell of each sample is identified by the name of the sample. Figure 8 shows the Cole-Cole plot for cell S10 for voltage bias ranging -1 mV to -544 mV. Figure 9 presents the equiva-

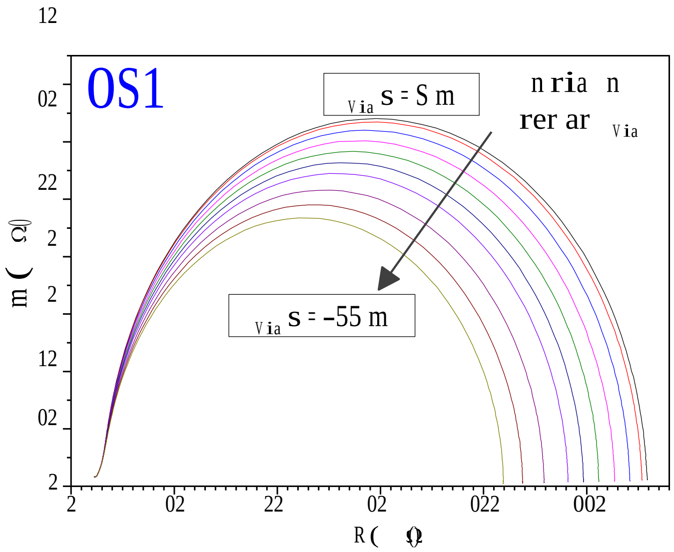

Figure 8: S10 sample complex impedance plane measurements for different applied voltage bias. The measurement were performed in dark conditions at room temperature, T=293K.

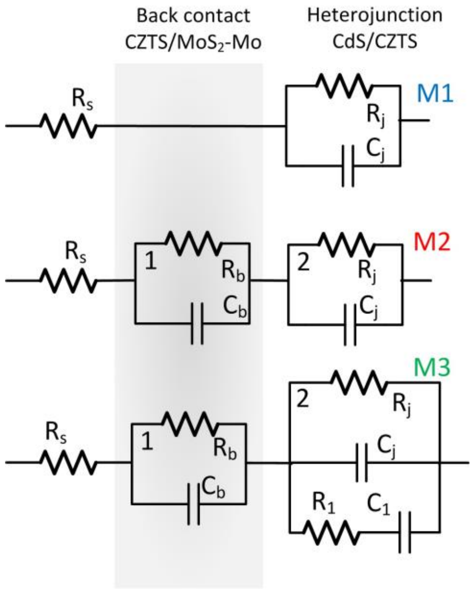

Figure 9: Tested solar cell equivalent circuits for the fitting of the complex admittance measurements in ac electrical regime.

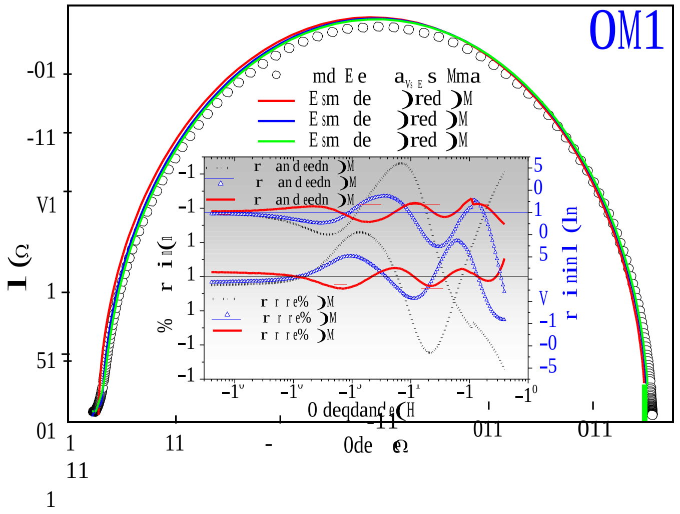

Figure 10: S10 sample complex impedance plane measurements for in dark conditions for a bias of -1 mV. This graphs presents the results of the fittings for the tested equivalent circuits. The inset graph shows the |Z| and Z phase fittings deviations for these tests.

lent circuits that were used to adjust the experimental admit- tance data [31]. The simplest circuit, M1, corresponds to a device characterized by a series resistance, R_s, and a parallel capacitance and resistance, C_j and R_j, respectively. The first element models all the contact and material resistances and the loop describes the CZTS/CdS heterojunction ac response. An extra loop is added for the circuit M2, formed by R_b and C_b which models the behaviour of a non-ohmic MoS$_2$-Mo/CZTS back contact. Further improvements are observed using model M3 which includes an extra parallel connection formed by a $C_1 - R_1$ pair, which describe the ac response of a trap state within p-n junction [32]. The results for the fittings are pre- sented in Figure 10. These graphs show that the best results are attained for the M3. It can also be observed that the experimen- tal data forms a slightly depressed semicircle when compared with the fittings. This impedance overestimation can be related with absorber layer inhomogeneity and low quality heterointer- face [32, 33]. Although there is the possibility to use constant phase elements to improve the results, they were no included in the equivalent circuits. The inset graphs of Figure 10 show the $|Z|$ and Z phase fitting errors *vs.* frequency. These results show a fitting improvement from model M1 to M3. For a low frequency regime, $f < 10^3$ Hz, all model present satisfactory fitting results. In this regime the ac response of the device is dominated by the capacitance of the junction, C_j. To improve the fittings for a higher frequency regime, the back contact loop must be added, as shown in model M2. Note that the maximum fitting error decrease from ≈17 % to ≈6 %. In this regime the capacitance behaviour of the solar cell is given by the relation $C = (1/C_j + 1/C_b)^{-1}$ [33]. The inclusion of a trap state reduces the error below 2%.

The extracted circuit parameters for the best solar cell of sample S10 are presented in Figure 11. These results show a constant series resistance of 7 Ω for dc bias ranging -0.6 V to 0 V. An apparent constant value close to 5 Ω is also presented by the back contact shunt resistance. The back contact capacitance

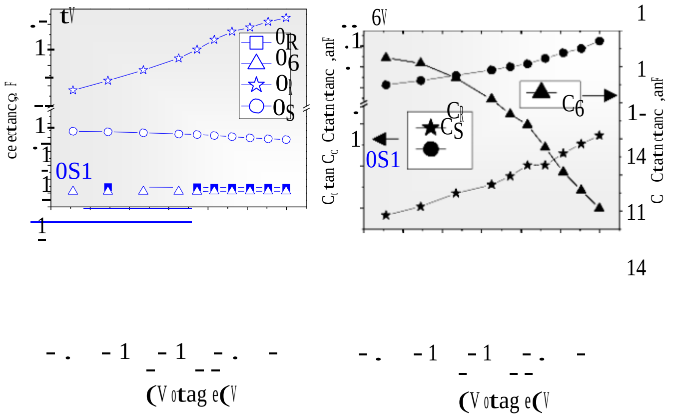

Figure 11: a) Resistances and b) capacitances for sample S10 under different applied dc bias. These values were estimated using non-linear fitting techniques based on Model M3.

values show a decrease with increasing reverse bias. This may suggest a directly polarized junction at the MoS2-Mo/CZTS interface. Note that assuming the junction area , A, equal to 0.25 cm^2 and the dielectric constant, ε, equal to 4.3 [34], a narrow depleted junction, $w_b = \varepsilon_0 \varepsilon A/C_b \simeq 15$ nm, is expected due to the relatively high observed capacitances. The junction capacitance shows the typical behaviour of a reversely polarized p-n junction, with values increasing from 11.7 nF to 15.5 nF. The shunt resistance, R_j, shows a clear dependence on the applied bias voltage and it may be related with the leakage paths which can physically originate from generation/recombination currents within the depletion region [35]. The interpretation of the two elements pertaining to the ac shunt R_1 and C_1 is not straightforward. The need to add these elements to the model may stem on the nonuniformity of the CZTS absorber layer. As shown in section 3.2, several secondary phases were detected in the absorber layer. Among them, there are relatively low resistivity phases such as Cu_4SnS_4 and $Cu_{41}Sn_{11}$ (not detected in S10) that could generate conduction channels through the absorber layer. This connection with the low resistivity phases is supported by the value of R_1, which is below 28 Ω. Even lower values were obtained for S30 and S60 due to the presence of the metallic phase $Cu_{41}Sn_{11}$. This shuntlike defect which can create leakage of the ac current through the devices may hide other

trap levels from the impedance measurements. Despite having been formed by different routes and phases, similar defects were detected on CdTe based devices [32]. An admittance-temperature study may confirm the high conductivity or metallic nature of these defects.

Figure 12 shows the Mott-Schottky plots based on the value of the junction capacitance, C_j, for the cells S10, S30 and S60. Using the data extracted from the linear regression and assuming an abrupt heterojunction, the estimation of the p-region ionized net acceptor defect concentration, N_a, and the overall built-in voltage, V_b, could be made according the following expression [36]:

$$\frac{A^2}{C_j^2} = \frac{2}{q\varepsilon_0\varepsilon_{CdS}\varepsilon_{CZTS}} \frac{N_d\varepsilon_{CdS} + N_a\varepsilon_{CZTS}}{N_aN_d}(V_b - V) \qquad (3)$$

where A is the junction area, q is the elementary charge, ε_0 is the vacuum permittivity, N_d is the n-region net ionized donor defect concentration, $= 1\times10^{17}$ cm^{-3} [37], ε_{CdS} is the CdS relative dielectric constant, = 5.4 [36], and ε_{CZTS} is the CZTS relative

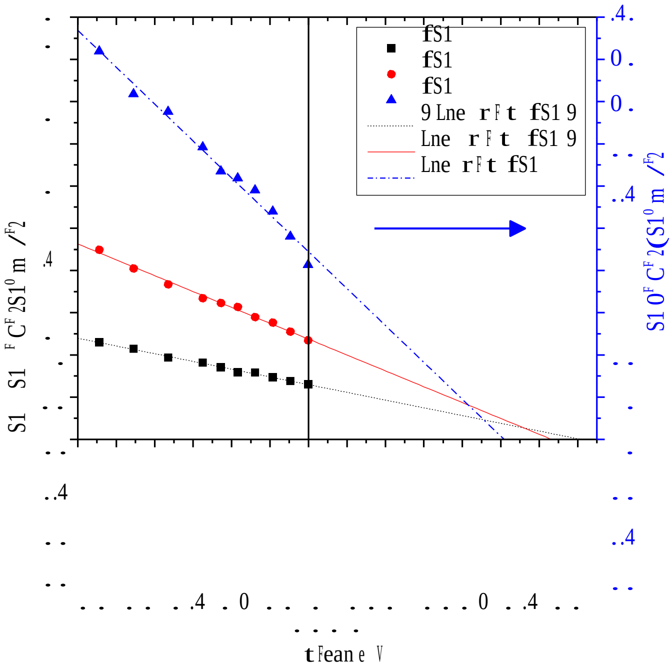

Figure 12: Mott-Schottky plots for the cells S10, S30 and S60 under reverse dc bias, -1 mV and -544 mV, in dark conditions at room temperature.

cell	N_a ($\times10^{16}$ cm^{-3})	V_b (V)	W_n (nm)	W_p (nm)
S10	20.0	0.71	60	30
S30	4.3	0.65	40	90
S60	0.65	0.51	20	230

Table 5: Estimated values for the majority carrier density, N, diffusion potential, V_b, and depletion width, W for samples S10, S30 and S60.

V_b are shown in Table 5. These values show a clear decrease of the acceptor doping density with increasing sulphurization time. Comparing with the literature, the values of N_a fall in the range of published data [4, 15, 39]. The depletion widths for p- and n-region, W_p and W_n, respectively, were obtained according the expression [36]:

$$W_{p\frown n} = \sqrt{\frac{2\varepsilon_0\varepsilon_{CdS}\varepsilon_{CZTS}}{q(N_d\varepsilon_{CdS} + N_a\varepsilon_{CZTS})} \frac{N_{d\frown a}}{N_{a\frown d}}(V_b - V)} \qquad (4)$$

ɔ 230 nm. The latter is comparable to the depletion width presented by Scragg *et al.* [15]. An inverse trend is presented by W_n from 60 nm to 20 nm. Note that, for S10 cell, the n-region of the heterojunction is considered fully depleted due to the thickness of the CdS layer of 50-70 nm. Analysing the built-in potentials values, it can be observed that they follow a similar trend to W_n. The estimated V_b are slightly higher than those reported in literature for similar free carrier concentration [4]. The decrease of V_b with the decrease of the acceptor doping concentration is expected. The observed decrease in acceptor density results from the general improvement in morphology and depth

dielectric constant, = 6.7 [38]. The estimated results for N_a and compositional uniformity, thus leading to lower grain boundary area and less intra-grain defects. In particular, the improvement in the depth compositional uniformity may lead to a reduction in Cu vacancies since the bottom of the films becomes less Cu- poor as the sulphurization time is increased.

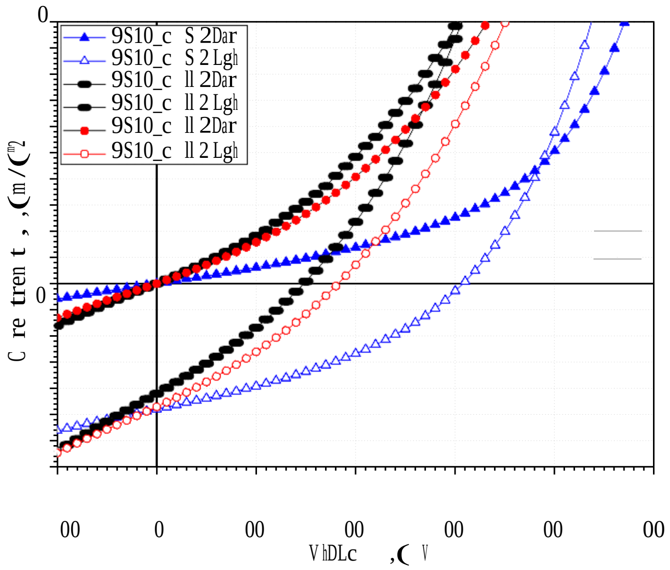

Figure 13: Solar cell J - V characteristics for the samples S10, S30 and S60 under simulated AM1.5 illumination and in dark conditions.

Param./cell	S10	S30	S60
Cell area (cm^2)	0.5	0.5	0.5
Fill factor (%)	36.4	29.1	30.3
V_{oc} (mV)	308	148	182
J_{sc} (mA/cm^2)	4.80	4.21	4.71
Efficiency (%)	0.54	0.18	0.26
R_s (Ω)	2.05	1.96	2.02
R_{sh} (Ω)	249	92	112

Table 6: Solar cell parameters for the cell S10, S30 and S60.

3.6. J-V characteristics

In Figure 13, the J-V characteristics of the cells S10, S30 and S60. All the cells show cross-over features, which means a low shunt resistance and this can be related to non ideal p-n junction properties or some photoconductive shunt. This low shunt resistance is observed in the Table 6. This Table shows that the S10 presents the best solar cell efficiency with 0.54%. The short circuit current density, J_{sc}, is low for all cells but no relevant differences between the cells are noted. However, the open circuit voltage, V_{oc}, and the shunt resistance, R_{sh}, present higher values for the S10 when compared to the other 2 cells.

The series resistance, R_s, shows low values, $\simeq 2.0$ Ω, with no important variation for the analysed cells.

4. Conclusions

In this paper it has been shown that by increasing the sulphurization time of metallic precursors there is an improvement of the in-depth homogeneity of the composition of the resulting CZTS thin films. Additionally, the structural and morphological properties are also enhanced due to the increase of crystallites and grain size. With regards to the electrical properties, the results show that with increasing sulphurization time there is a lower free carrier concentration, a wider space charge region and higher conduction activation energy. From a solar cell point of view, the increase of the depletion width will increase the resulting J_{sc} of the solar cell if the material has collection losses. The influence of decreasing the carrier concentration is difficult to evaluate, if on one hand the Auger recombination will decrease and therefore this would provide a higher life- time of the minority carriers and therefore an increased V_{oc}, on the other hand the lower carrier concentration could drop the V_{oc} due to the lower resulting V_b. Since the electrical changes are not the only ones seen in this work, the evaluation of these changes in the electrical performance is quite hard. It was also observed that for longer sulphurization times a Cu_xSn_y metal alloy is formed. This explains the lower shunt resistance and lower open circuit voltages observed. This work suggests that in order to avoid the formation of this metal alloy one should reduce the thickness of the films thus allowing a sulphurization time reduction for similar in-depth uniformity.

5. Acknowledgements

This work is supported by the projects PTDC/CTM-MET/113486/2009 and PEst-C/CTM/LA0025/2011 funded by Fundação para a Ciência e Tecnologia (FCT). FCT is also acknowledged for the financial support of the national electronic microscopy network, whose services we have used, through the grant REDE/1509/RME/2005. We would also like to acknowl- edge the financial support of FCT and the Brazilian agency CAPES to this project through the grants 411.00 and 3779-08- 4, respectively. The authors also thank the bilateral collabora- tion project FCT/DAAD.

[1] J.M. Raulot, C. Domain , J.F. Guillemoles, *Ab initio investigation of po- tential indium and gallium free chalcopyrite compounds for photovoltaic application*, Journal of Physics and Chemistry of Solids, 66, (2005), 2019.

[2] P.A. Fernandes, P.M.P. Salomé, A.F. da Cunha, *Cu_xSnS_{x+1} ($x = 2, 3$) thin films grown by sulfurization of metallic precursors deposited by dc magnetron sputtering*, Phys. Status Solidi (c), 7, (2010), 901.

[3] J.P. Leitão, N.M. Santos, P.A. Fernandes, P.M.P. Salomé, A.F. da Cunha, J.C. González, F.M. Matinaga, *Study of optical and structural properties of Cu_2ZnSnS_4 thin films*, Thin Solid Films, Thin Solid Films, 519, (2011), 73907393.

[4] B. Shin, O. Gunawan, Y. Zhu, N. A. Bojarczuk, S. J. Chey and S. Guha, *Thin film solar cell with 8.4% power conversion efficiency using an earth- abundant Cu_2ZnSnS_4 absorber*, Prog. Photovolt: Res. Appl., (2011), DOI: 10.1002/pip.1174.

[5] P. Jackson, D. Hariskos, E. Lotter, S. Paetel, R. Wuerz, R. Men- ner, W. Wischmann, and M. Powalla, *New world record efficiency for Cu(In,Ga)Se_2 thin-film solar cells beyond 20%*, Prog. Photovoltaics Res. Appl., (2011), doi: 10.1002/pip.1078.

[6] S. Chen, X.G. Gong, A. Walsh and S.-H. Wei, *Defect physics of the kesterite thin-film solar cell absorber Cu_2ZnSnS_4*, Appl. Phys. Lett., 96 (2010) 021902.

[7] H. Katagiri, K. Jimbo, M. Tahara, H. Araki, K. Oishi, in: A. Yamada, C. Heske, M. Contreras, M. Igalson, S.J.C. Irvine, *The influence of the composition ratio on CZTS-based thin film solar cells*, (Eds.), Thin-Film Compound Semiconductor Photovoltaics 2009, San Francisco, U.S.A., April 13-17, Mater. Res. Soc. Symp. Proc., 1165 (2009) 1165-M04-01.

[8] P.A. Fernandes, P.M.P. Salomé, A.F. da Cunha, *Growth and Raman scat- tering characterization of Cu_2ZnSnS_4 thin films*, Thin Solid Films, 517 (2009) 2519.

[9] T. M. Friedlmeier, H. Dittrich and H. W. Schock, *Growth and*

Characteri- zation of $Cu2ZnSnS4$ *and* $Cu2ZnSnSe4$ *Thin Films For Photocoltaic Appli- cations*, The 11th Conf. on Ternary and Multinary Compounds, ICTMC- 11 (Salford, UK, 8-12 September, (1997), 345.

[10] H. Katagiri, K. Saitoh, T. Washio, H. Shinohara, T. Kurumadani and S. Miyajima, *Development of thin film solar cell based on* $Cu2ZnSnS4$ *thin films*, Solar Energy Mater. Solar Cells, 65, (2001), 141.

[11] T. Tanaka, D. Kawasaki, M. Nishio, Q. Guo and H. Ogawa, F*abrication of Cu2ZnSnS4 thin films by co-evaporation*, Phys. Status Solidi (c), (2006), 3, 2844.

[12] Björn-Arvid Schubert, Björn Marsen, Sonja Cinque, Thomas Unold, Reiner Klenk, Susan Schorr and Hans-Werner Schock, C*u2ZnSnS4 thin film solar cells by fast coevaporation*, Prog. Photovolt: Res. Appl., 19, (2010), 93.

[13] P. A. Fernandes, P. M. P. Salomé and A. F. da Cunha, *Precursors order effect on the properties of sulfurized Cu2ZnSnS4 thin films*, Semicond. Sci. Technol. 24, (2009), 105013.

[14] K. Tanaka, N. Moritake and H. Uchiki, *Preparation of Cu2ZnSnS4 thin films by sulfurizing solgel deposited precursors*, Solar Energy Mater. So- lar Cells, 91 (2007) 1199.

[15] J. J. Scragg, P. J. Dale and L. M. Peter, *Synthesis and characterization of Cu2ZnSnS4 absorber layers by an electrodeposition-annealing route*, Thin Solid Films, 517 (2009) 2481.

[16] A. Ennaoui, M. Lux-Steiner, A. Weber, D. Abou-Ras, I. Ktschau, H.-W. Schock, R. Schurr, A. Hlzing, S. Jost, R. Hock, T. Voß, J. Schulze, A. Kirbs, *Cu2ZnSnS4 thin film solar cells from electroplated precursors: Novel low-cost perspective*, Thin Solid Films, 517 (2009) 2511.

[17] T. Todorov, M. Kita, J. Carda and P. Escribano, *Cu2ZnSnS4 films de- posited by a soft-chemistry method*, Thin Solid Films, 517 (2009) 2541.

[18] N. Nakayama and K. Ito, *Sprayed films of stannite Cu2ZnSnS4*, Appl. Surf. Sci., 92 (1996) 171.

[19] N. Kamoun, H. Bouzouita and B. Rezig Thin Solid Films, *Fabrication and characterization of Cu2ZnSnS4 thin films deposited by spray pyrolysis technique*, 515, (2007), 5949.

[20] P. M. P. Salomé, J. Malaquias, P. A. Fernandes and A. F. da Cunha, *Mo bilayer for thin film photovoltaics revisited*, J. Phys. D: Appl. Phys. 43 (2010) 345501.

[21] P. A. Fernandes, P. M. P. Salomé and A. F. da Cunha, *A study of ternary Cu2SnS3 and Cu3SnS4 thin films prepared by sulfurizing stacked metal precursors*, J. Phys. D: Appl. Phys., 43, (2010), 215403.

[22] P. A. Fernandes, P. M. P. Salomé and A. F. da Cunha, *Study of polycrys- talline Cu2ZnSnS4 films by Raman scattering*, J. Alloys Compd., 509, (2011), 7600.

[23] X. Fontané, L. Calvo-Barrio, V. Izquierdo-Roca, E. Saucedo, A. Pérez- Rodriguez, J. R. Morante, D. M. Berg, P. J. Dale, and S. Siebentritt, *In- depth resolved Raman scattering analysis for the identification of sec- ondary phases: Characterization of Cu2ZnSnS4 layers for solar cell ap- plications*, Appl. Phys. Lett., 98, (2011), 181905

[24] International Centre for Diffraction Data - Ref. Code, 01-075-4122 (Cu2ZnSnS4), 04-003-2919 (Mo), 33-1375 (SnS), 09-0312 (MoS2), 1- 071-7876 (Cu41Sn11) and 00-029-0584 (Cu4SnS4)

[25] M. Altosaar, J. Raudoja, K. Timmo, M. Danilson, M. Grossberg, J. Krus- tok, and E. Mellikov, *Cu2Zn1−xCdxSn(Se1−ySy)4 solid solutions as ab- sorber materials for solar cells*, phys. stat. sol. (a), 205, No. 1, (2008), 167.

[26] S. Jiménez Sandoval, D. Yang, R. F. Frindt and J. C. Irwin, *Raman study and lattice dynamics of single molecular layers of MoS2*, Physical Review B, 44, (1991), 3955.

[27] J. Scragg,*Studies of Cu2ZnSnS4 films prepared by sulfurisation of elec- trodeposited precursors*,PhD dissertation, University of Bath, (2010).

[28] C. E. Kril and R. Birringer, *Estimating grain-size distributions in nanocrystalline materials from X-ray diffraction profile analysis*, Phil. Mag. A, 77, (1998), 621.

[29] J. P. Leitão, N. M. Santos, P. A. Fernandes, P. M. P. Salomé, A. F. da Cunha, J. C. Gonzlez, G. M. Ribeiro, and F. M. Matinaga, *Photolumines- cence and electrical study of fluctuating potentials in Cu2ZnSnS4-based thin films*, Phys. Rev. B, 84, (2011), 024120

[30] P. C. Mathur, R. P. Sharma, Renuka Shrivastava, P. Saxena, and R. K. Kotnala, *Temperature dependence of electrical transport properties of n- type solar grade polycrystalline silicon*, J. Appl. Phys., 54,(1983), 3913.

[31] P. A. Fernandes, A. F. Sartori, P. M. P. Salomé, J. Malaquias, A. F. da Cunha, M. P. F. Graça and J. C. González, *Admittance spectroscopy of Cu2ZnSnS4 based thin film solar cells*, Appl. Phys. Lett., 100 (2012) 233504.

[32] Y. Y. Proskuryakov, K. Durose, B. M. Taele and S. Oelting, *Impedance spectroscopy of unetched CdTe/CdS solar cellsequivalent circuit analysis*, J. Appl. Phys.,102, (2007), 024504.

[33] Evgenij Barsoukov and J. Ross Macdonald, *Impedance Spectroscopy*

Theory, Experiment, and Applications, John Wiley and Sons, Inc., Hobo- ken, New Jersey, 2005.

[34] R. Schlaf, O. Lang, C. Pettenkofer, and W. Jaegermann, *Band lineup of layered semiconductor heterointerfaces prepared by van der Waals epi- taxy: Charge transfer correction term for the electron affinity rule*, J. Appl. Phys., 85, (1999), 2732.

[35] W.A. Strifler and C.W. Bates, *Admittance spectroscopy of* $CuInSe_2/CdS$ *solar cells prepared by chemical spray pyrolysis*, J. Appl. Phys., 71, (1992), 4358.

[36] S. M. Sze and Knok K. Ng, *Physics of Semiconductor Devices*, 3rd Edi- tion, Wiley-Interscience, chap.2, (2007).

[37] M. Gloeckler, *Numerical Modeling of CIGS Solar Cells: Definition of the Baseline and Explanation of Superposition Failure*, Master Thesis, Colorado, (2003).

[38] Clas Persson, *Electronic and optical properties of* Cu_2ZnSnS_4 *and* $Cu_2ZnSnSe_4$, J. Appl. Phys. 107, (2010), 053710.

[39] D. B. Mitzi, O. Gunawan, T. K. Todorov, K, Wang, S, Guha, *The path towards a high-performance solution-processed kesterite solar cell*, Solar Energy Mater. Solar Cells, 95, (2011), 1421.